Home   Search   Collections   Journals   About   Contact us   My IOPscience

Crystal structure and electronic properties of the $Ag_2V_4O_{11}$ insertion electrode

Crystal structure and electronic properties of the $Ag_2V_4O_{11}$ insertion electrode

Masashige Onoda and Keisuke Kanbe

Institute of Physics, University of Tsukuba, Tennodai, Tsukuba 305-8571, Japan

Abstract
The crystal structure and electronic properties of $Ag_2V_4O_{11}$ have been explored
by means of x-ray four-circle diffraction and through measurements of electrical
resistivity, thermoelectric power, magnetization, and electron paramagnetic
resonance. The crystal data for the nearly stoichiometric compound show
a monoclinic structure with space group $C2/m$; $a = 15.480(3)$ Å, $b = 3.582(1)$ Å, $c = 9.537(2)$ Å, $\beta = 128.741(9)°$, and $Z = 2$. The structure
at 293 K determined with residual factors of $R = 0.055$ and $R_w = 0.051$ is
described as the stacking of layers formed by sharing edges and corners of
distorted VO_6 octahedra. The transport mechanism of 3d electrons donated
by the slight deficiency of oxygen atoms is understood as a small-polaron
conduction in the localized states of band tails.

1. Introduction

Transition-metal oxides have aroused considerable interest both from the basic science and
the applied viewpoints. For example, the layered ternary oxides with unfilled d orbitals have
been investigated in order to clarify properties of correlated electron systems and quantum
spin-fluctuation systems. On the other hand, they can be utilized as cathode materials in
rechargeable lithium batteries in view of their structural suitability for undergoing intercalation
and deintercalation with lithium ions. In principle, the discharge–charge process of the batteries
should correspond to the reduction–oxidation process of cathode materials or transition-metal
ions. Therefore, it will be possible to study detailed properties of the layered system as a
function of the concentration of d electrons from the basic science viewpoint, unless that
reaction suffers a multiphase separation.

A silver vanadium oxide with the chemical formula $Ag_2V_4O_{11}$ has been used as the primary
power source for implantable biomedical devices [1]. It has also been found that, depending on
the oxygen deficiency, around six or seven lithium ions are intercalated via an electrochemical
reaction, and this process is reversible [2, 3]. The structure determination for $Ag_2V_4O_{11}$ was
performed with high-resolution electron microscopy and x-ray powder diffraction [4, 5]. Two
silver-deficient structural models which consist of V_4O_{11} layers have been proposed: one

(type I) has a $C2/m$ cell with dimensions $a = 15.41$ Å, $b = 3.5766$ Å, $c = 9.564$ Å, and $\beta = 128.74°$. Another C-centred monoclinic cell (type II) has dimensions $a = 15.3$ Å, $b = 3.60$ Å, $c = 7.6$ Å, and $\beta = 102°$, closely related to the values for $Cu_{2-x}V_4O_{11}$ [6–8]. The difference between the structures of types I and II was attributed to that of the stackings of the V_4O_{11} layers along the c^*-direction. It is noted that these models may lead to a higher oxidation state of the silver ions, Ag^{2+} or Ag^{3+}, from charge balance, since the stoichiometric composition $Ag_2V_4O_{11}$ is expected to be a band insulator for all valences of Ag^+, V^{5+}, and O^{2-}. No report on the physical properties of $Ag_2V_4O_{11}$ has been published.

Vanadium pentoxide V_2O_5 is known to be an n-type semiconductor; this feature arises from the oxygen vacancies [9]. Thus, the V ions are in a V^{4+}–V^{5+} mixed-valence state, and small polarons are formed due to a strong electron–phonon coupling. It is interesting to explore the electronic properties of $Ag_2V_4O_{11}$ from such a viewpoint. Section 2 describes the crystal structure determined by means of single-crystal x-ray diffraction, and in section 3, the electronic properties revealed through measurements of electrical resistivity, thermoelectric power, magnetization, and electron paramagnetic resonance (EPR) are discussed. Section 4 is devoted to conclusions.

2. Crystal structure

2.1. Sample preparation, chemical analysis, and lattice constants

To obtain polycrystalline specimens, mixtures of Ag_2O (99.9% purity) and V_2O_5 (99.99% purity) were ground and pressed into pellets, and then sintered in air or an oxygen atmosphere at various temperatures between 673 and 798 K. The attempted preparation from a congruent melt at temperatures above 843 K was unsuccessful. Electron-probe microanalysis (EPMA) and x-ray powder diffraction were performed at room temperature using a JEOL JAX-8621 and a Rigaku RAD-IIC diffractometer with Cu Kα radiation, respectively.

The specimens sintered at 798 K in air and the oxygen atmosphere, hereafter called specimens (A) and (O), respectively, were both assemblies of sizable crystallites of $Ag_2V_4O_{11}$ (type I) as pointed out previously [10]. Using the powder diffraction pattern calculated on the basis of the atomic parameters described later, the lattice constants for specimen (A) are $a = 15.442(5)$ Å, $b = 3.5792(7)$ Å, $c = 9.515(2)$ Å, and $\beta = 128.72(2)°$; and those for (O) are $a = 15.485(4)$ Å, $b = 3.5839(5)$ Å, $c = 9.537(2)$ Å, and $\beta = 128.79(2)°$. They are similar to those of type I [5]. A small amount of impurity powder of $Ag_{1+x}V_3O_8$ adhered to the cleavage plane and it was easily removed. Below that temperature, 798 K, the crystallites became poor and the amount of $Ag_{1+x}V_3O_8$ phase present increased significantly. For the conditions of sample preparation described here, type II did not appear, inconsistently with the recent structural work [4, 5]. The EPMA analysis for the specimens (A) and (O) indicated that the Ag and V concentrations are 1.99(1) and 4.000(3), respectively, independently of the atmospheric conditions. Therefore, silver deficiency is found to be absent within experimental accuracy.

2.2. Structure determination

The x-ray four-circle diffraction measurements were performed on a Rigaku AFC-7R (custom-made) diffractometer with graphite-monochromated Mo Kα radiation at 293 K. The crystal with dimensions of $0.18 \times 0.12 \times 0.02$ mm made in air was mounted on a glass fibre. The crystal was (0 0 1) twinned for the lattice constants described below. As a result of setting each orientation matrix precisely, only reflections from the single domain were obtained.

The intensity data were collected over a maximum 2θ range of $90°$ using the ω–2θ scan technique. Of 1488 unique reflections from the single domain with removal of the overlapped reflections due to the twinning, 1057 reflections with $|F_o| \geqslant 3\sigma$, F_o and σ being the observed structure factor and its standard deviation, respectively, were used. Lorentz polarization, the absorption correction, and the secondary extinction correction were applied, where the transmission factors were in the range 0.36–0.82. The internal consistency of the reflections was estimated on the basis of F_o^2 to be $R_{int} = 0.052$.

Through the systematic absences of reflections, a statistical analysis of the intensity distribution, and the successful solution and refinement of the structure, the crystal data were determined as: monoclinic with space group $C2/m$ (No 12); $a = 15.480(3)$ Å, $b = 3.582(1)$ Å, $c = 9.537(2)$ Å, $\beta = 128.741(9)°$, $V = 412.5(2)$ Å^3, and $Z = 2$; μ(Mo Kα) $= 9.041$ mm^{-1}; and $D_{cal} = 4.794$ Mg m^{-3}. The dimensions agree well with those estimated for specimen (O) by means of the x-ray powder diffraction. Large crystallites may have these dimensions regardless of the atmosphere. It is noted that there are alternative settings for the monoclinic unit cells: $a' = 15.293(3)$ Å, $b' = 3.582(1)$ Å, $c' = 9.537(2)$ Å, and $\beta' = 127.859(9)°$, on the basis of the following relation:

$$\begin{pmatrix} a' \\ b' \\ c' \end{pmatrix} = \begin{pmatrix} 1 & 0 & 2 \\ 0 & -1 & 0 \\ 0 & 0 & -1 \end{pmatrix} \begin{pmatrix} a \\ b \\ c \end{pmatrix}. \tag{1}$$

The structure was solved by direct methods [11], expanded using Fourier techniques, and refined by full-matrix least-squares calculations with anisotropic displacement parameters. The atomic scattering factors were taken from reference [12], and anomalous dispersion effects were included using the values given by reference [13]. The residual factors defined as

$$R = \left[\sum (|F_o| - |F_c|)^2 \right] / \left(\sum |F_o| \right) \tag{2}$$

and

$$R_w = \left\{ \left[\sum w(|F_o| - |F_c|)^2 \right] / \left(\sum w F_o^2 \right) \right\}^{1/2} \tag{3}$$

where $|F_c|$ is a calculated structure factor, are finally[1] $R = 0.055$ and $R_w = 0.051$. All of the calculations were performed using the teXsan crystallographic software package [14].

The atomic coordinates, equivalent isotropic thermal parameters, and anisotropic displacement parameters are listed in table 1. Selected interatomic distances are listed in table 2. The atomic coordinates determined here are roughly consistent with the previous result [5], but significant deviations over 1×10^{-2} exist for oxygen atoms O3 and O6. Thus, the interatomic distances for these atoms are significantly different from those presented previously. Moreover, standard deviations in this work are greatly improved. Figure 1 indicates the crystal structure projected on the ac-plane with the polyhedral scheme. There exist two independent vanadium atoms labelled V1 and V2. The V1–O and V2–O bond lengths range from 1.612 to 2.243 Å and from 1.622 to 2.414 Å, respectively, indicating that each V atom forms a distorted octahedron. Thus, the structure is described in terms of the $V1O_6$ and $V2O_6$ octahedra which are joined by sharing edges and corners to form the V_4O_{11} layers in the ab-plane.

The V1 and V2 ions are both close to pentavalent according to the bond-length–bond-strength relation [15]. The ground-state wavefunctions for the $V1O_6$ and $V2O_6$ octahedra are composed of $0.987d_{xy} - 0.156d_{yz}$ and $0.968d_{yz} - 0.247d_{xy}$, respectively, where $x \parallel a^*$ and $y \parallel b$, where we have used the Hartree–Fock function for V^{4+} [16].

---

[1] Supplementary data files are available from the article's abstract page in the online journal; see http://www.iop.org.

Table 1. Atomic coordinates, equivalent isotropic thermal parameters B_{eq} (Å^2), and anisotropic displacement parameters U_{ij} of Ag$_2$V$_4$O$_{11}$ at 293 K, where $y = 0$ and $U_{12} = U_{23} = 0$ for all of the atoms. B_{eq} and U_{ij} are defined by $B_{eq} = \frac{8}{3}\pi^2[U_{11}(aa^*)^2 + U_{22}(bb^*)^2 + U_{33}(cc^*)^2 + 2U_{12}aa^*bb^*\cos\gamma + 2U_{13}aa^*cc^*\cos\beta + 2U_{23}bb^*cc^*\cos\alpha]$, and the parameters are defined in the thermal factor form $T = \exp[-2\pi^2(a^{*2}U_{11}h^2 + b^{*2}U_{22}k^2 + c^{*2}U_{33}l^2 + 2a^*b^*U_{12}hk + 2a^*c^*U_{13}hl + 2b^*c^*U_{23}kl)]$.

Atom	x	z	B_{eq}	U_{11}	U_{22}	U_{33}	U_{13}
Ag	0.11973(5)	0.51088(9)	1.71(1)	0.0301(4)	0.0168(3)	0.0206(3)	0.0171(3)
V1	0.1493(1)	0.1432(2)	1.17(2)	0.0210(5)	0.0105(6)	0.0178(5)	0.0145(5)
V2	0.36639(9)	0.1501(1)	0.73(2)	0.0099(4)	0.0090(5)	0.0105(4)	0.0072(3)
O1	0	0	1.3(1)	0.010(3)	0.012(3)	0.023(4)	0.009(3)
O2	0.3453(4)	0.9071(7)	0.89(8)	0.008(2)	0.012(2)	0.013(2)	0.007(2)
O3	0.1671(4)	0.9272(7)	0.83(7)	0.013(2)	0.007(2)	0.015(2)	0.011(2)
O4	0.1805(4)	0.3393(8)	1.36(10)	0.018(2)	0.022(3)	0.017(2)	0.013(2)
O5	0.3245(4)	0.2816(7)	1.06(8)	0.013(2)	0.015(2)	0.015(2)	0.010(2)
O6	0.5003(4)	0.2993(8)	1.39(9)	0.009(2)	0.016(3)	0.024(3)	0.009(2)

Table 2. Selected interatomic distances (Å) and angles (deg) of Ag$_2$V$_4$O$_{11}$ at 293 K, where the translation codes are (i) x, y, z; (ii) $\frac{1}{2} - x, -\frac{1}{2} - y, 1 - z$; (iii) $\frac{1}{2} - x, \frac{1}{2} - y, 1 - z$; (iv) $x, y, -1 + z$; (v) $-\frac{1}{2} + x, -\frac{1}{2} + y, z$; (vi) $-\frac{1}{2} + x, \frac{1}{2} + y, z$; (vii) $x, -1 + y, z$; (viii) $x, 1 + y, z$; (ix) $\frac{1}{2} - x, \frac{1}{2} - y, -z$; (x) $\frac{1}{2} - x, -\frac{1}{2} - y, -z$; (xi) $-x, -y, -z$; (xii) $x, y, 1 + z$.

V1O$_6$ polyhedra		Ag(i)–O5(ii, iii)	2.394(4)
V1(i)–O1(i)	1.804(1)	Ag(i)–O6(v, vi)	2.455(4)
V1(i)–O2(ii, iii)	1.869(2)	V–V distances	
V1(i)–O3(iv)	2.243(5)	V1(i)–V1(vii, viii)	3.582(2)
V1(i)–O4(i)	1.612(5)	V2(i)–V2(ix, x)	3.388(2)
V1(i)–O5(i)	2.149(5)	V1(i)–V2(ix, x)	3.200(2)
V2O$_6$ polyhedra		V–O–V angles	
V2(i)–O2(iv)	2.129(5)	V1(i)–O1(i)–V1(xi)	180
V2(i)–O3(ii, iii)	1.882(2)	V1(ii)–O2(i)–V1(iii)	146.7(3)
V2(i)–O3(iv)	2.414(5)	V2(iii)–O3(i)–V2(ii)	144.2(3)
V2(i)–O5(i)	1.735(4)	V1(ii)–O2(i)–V2(xii)	106.2(1)
V2(i)–O6(i)	1.622(5)	V1(xii)–O3(i)–V2(ii)	101.4(1)
AgO$_5$ polyhedra		V1(xii)–O3(i)–V2(xii)	90.9(2)
Ag(i)–O4(i)	2.344(5)	V1(i)–O5(i)–V2(i)	117.1(3)

The Ag site is located between the V$_4$O$_{11}$ layers. The occupancy probability of Ag is 0.991(5), so the Ag vacancies are negligibly small, which is consistent with the EPMA analysis. On the assumption of a coordination sphere of 2.50 Å, the Ag ions are each surrounded with five O atoms. The Ag–O bond lengths range from 2.344 to 2.455 Å, leading to the average value of 2.408 Å. Thus, the ionic radius of Ag is estimated to be 1.028 Å, which agrees well with that for five coordinations of the Ag$^+$ ion [17].

3. Electronic properties

3.1. Magnetization

The magnetizations were measured by the Faraday method with a field of up to 1 T at temperatures between 4.2 and 300 K. The magnetic susceptibility χ was deduced from the linear part of the magnetization–field curve with a decreasing field.
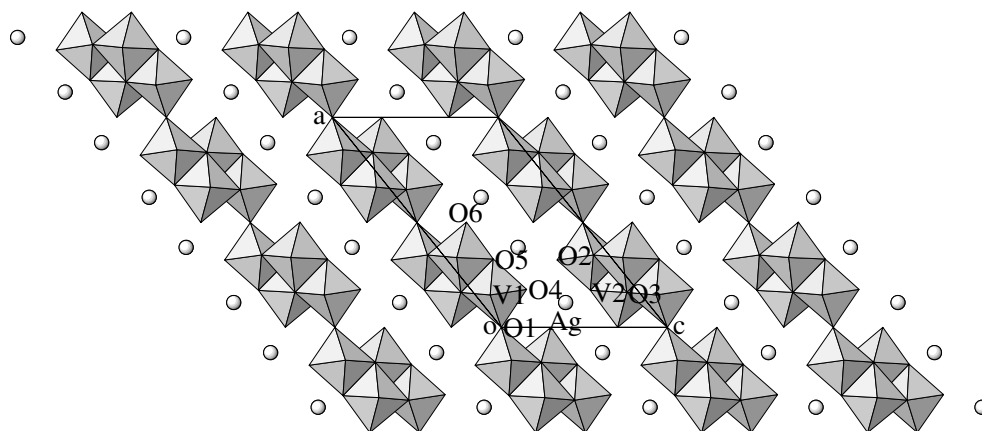
Figure 1. The crystal structure of $Ag_2V_4O_{11}$ projected on the ac-plane with the polyhedral scheme.

The temperature dependence of χ^{-1}, for the specimens (A) and (O), is shown in figure 2. For both of the specimens, χ is almost explained by considering the contributions of the Curie–Weiss-type susceptibility and the temperature-independent susceptibility of the Van Vleck orbital and diamagnetic components, χ_0:
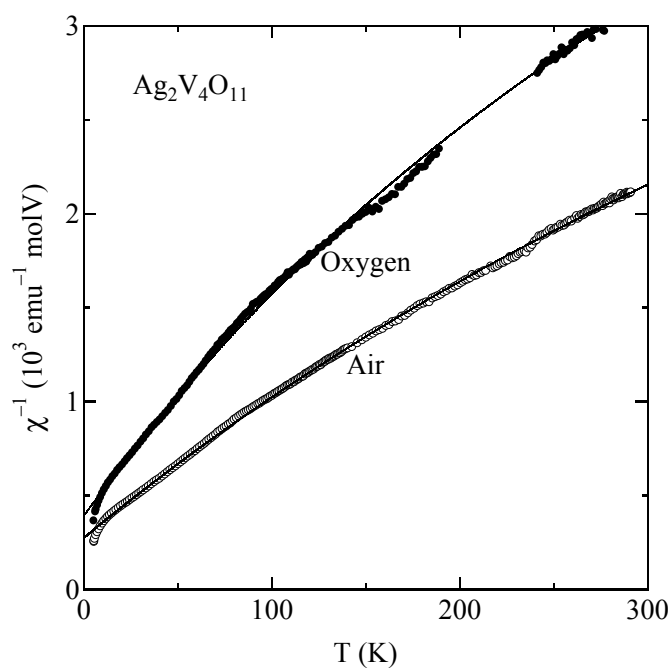
$$\chi = \frac{C}{T + T_W} + \chi_0 \tag{4}$$

Figure 2. The temperature dependence of the inverse of the magnetic susceptibility χ^{-1} for $Ag_2V_4O_{11}$ prepared in air and an oxygen atmosphere, where the full curves are drawn on the basis of equation (4).

where C and T_W are the Curie constant and the Weiss temperature, respectively. The full curves in figure 2 are drawn on the basis of the parameters $C = 7.02(4) \times 10^{-3}$ emu K (mol V)$^{-1}$, $T_W = 32.0(5)$ K, $\chi_0 = 3.13(5) \times 10^{-5}$ emu (mol V)$^{-1}$ for specimen (A), and $C = 4.13(4) \times 10^{-3}$ emu K (mol V)$^{-1}$, $T_W = 27.2(6)$ K, $\chi_0 = 2.89(4) \times 10^{-5}$ emu (mol V)$^{-1}$ for specimen (O). Since the Ag and V ions are in the ratio of 1:2 as described earlier, this temperature-dependent paramagnetism arises from the oxygen deficiencies of the specimens which are compensated by V ions in a lower oxidation state, V^{4+}. The V^{4+} ions have the space-averaged g-factor of 1.964 as will be described later, so the oxygen deficiencies δ defined in $Ag_2V_4O_{11-2\delta}$, δ being equal to the number of V^{4+} ions per mole of V, are 0.019 and 0.011, respectively. In spite of the rather low concentration of V^{4+}, the Weiss temperature appears not to be small, suggesting that the donated electrons are distributed not randomly but in a mass.

3.2. Electrical resistivity and thermoelectric power

The four-terminal electrical resistivity ρ and the thermoelectric power S were measured by a dc method in the temperature region between 130 and 300 K.

A plot of ρ as a function of the inverse temperature for the specimens (A) and (O) shown in figure 3 indicates that they are like semiconductors. From the full lines, the energy gap E_ρ defined by

$$\rho = \rho_0 \exp(E_\rho/T) \tag{5}$$

where ρ_0 is assumed to be a constant, is estimated to be 1076(1) and 1062(1) K for the specimens (A) and (O), respectively. The energy gaps estimated at low temperatures are somewhat larger than those at high temperatures.
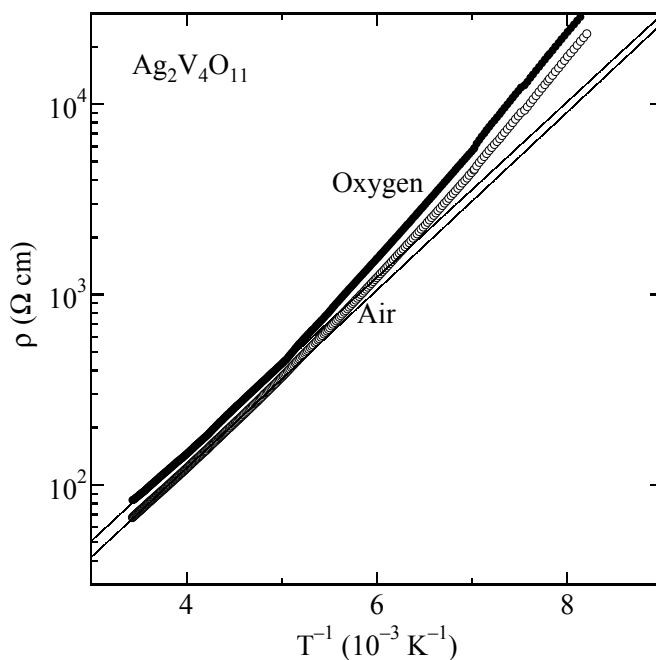

Figure 3. The temperature dependence of the electrical resistivity ρ for $Ag_2V_4O_{11}$ prepared in air and an oxygen atmosphere, where the full lines are drawn on the basis of equation (5).

Figure 4 shows S-data against the inverse temperature for the specimens (A) and (O). Both sets of data obey the following empirical model with electron carriers:

$$S = -eE_S/T + S_0 \tag{6}$$

where E_S is the gap and S_0 is a constant. The full lines in this figure give $E_S = 580(3)$ K and $S_0 = -242(1)$ μV K^{-1} for specimen (A), and $E_S = 481(2)$ K and $S_0 = -269(1)$ μV K^{-1} for specimen (O). These gap energies are significantly smaller than those obtained for the resistivity. This result may be characteristic of small-polaron motion and it is basically understood by considering the narrow tails of localized states which extend into the forbidden gap and a band of compensated levels originating from the oxygen vacancies near the middle of the gap [18, 19]. Here, the width between the energies at the Fermi level and at the tail edge is represented by ΔE. When the wavefunctions are localized, conduction can only occur via thermally excited hopping with a phonon-exchange energy E_p. Then, the resistivity is approximately given by equation (5), where $E_\rho = \Delta E + E_p$. On the other hand, the thermoelectric power is expressed by equation (6) with $E_S = \Delta E$. Thus, the activation energy estimated from the resistivity is the sum of the energies for carrier creation and for hopping, and the energy for hopping does not appear in the thermoelectric power. Then, E_p is deduced to be 496 K for specimen (A) and 581 K for specimen (O). Although a small temperature dependence of the pre-exponential term ρ_0 should be considered in order to estimate E_ρ precisely, this is difficult, since the temperature region measured is not wide.
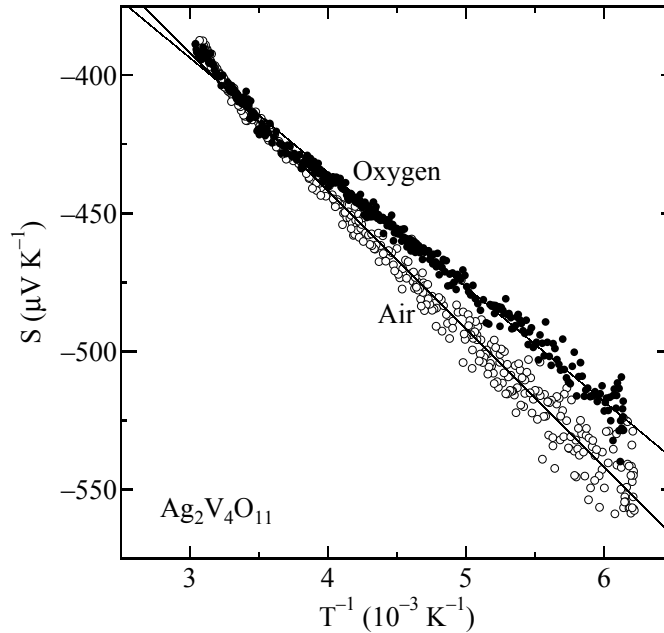

Figure 4. The temperature dependence of the thermoelectric power S for Ag$_2$V$_4$O$_{11}$ prepared in air and an oxygen atmosphere, where the full lines are drawn on the basis of equation (6).

In the high-temperature limit where the fraction of V sites c occupied by mobile electrons is fixed, S_0 in equation (6) approximately corresponds to the so-called Heikes formula [20]:

$$S_p = \frac{k}{e} \ln\left(\frac{c}{1-c}\right) \tag{7}$$

where k is the Boltzmann coefficient. Taking account of the magnetization results, this formula gives values of -338 and $-384\,\mu\text{V K}^{-1}$ for the specimens (A) and (O), respectively, which are qualitatively consistent with the experimental results.

3.3. Electron paramagnetic resonance

EPR measurements for the specimens (A) and (O) were performed at temperatures between 5 and 300 K at 9.03 GHz using a JEOL TE200 spectrometer. The spectra were asymmetric and their temperature dependences were similar for the specimens (A) and (O) in the measurement region. The spin susceptibility extracted on the basis of the integration of the signal, taking account of the temperature dependence of a Q-factor, was almost consistent with the Curie–Weiss contribution in equation (4). Examples of the spectra at 273.0 and 76.0 K for specimen (O) are shown in figure 5. The asymmetric spectra are explained as shown by the full curves in figure 5 on the assumption that the g-factor and the peak-to-peak linewidth, W, with the shape of a Lorentzian, have uniaxial angular dependences as follows:

$$g^2 = g_{XY}^2 \sin^2\theta + g_Z^2 \cos^2\theta \tag{8}$$

$$W = W_{XY} \sin^2\theta + W_Z \cos^2\theta \tag{9}$$

where θ is the angle of the direction of the external field with respect to the principal axis $\mathbf{Z}$ of the g- and W-tensors, and $g_{Z(XY)}$ and $W_{Z(XY)}$ express the principal values parallel (perpendicular) to the $\mathbf{Z}$-direction. The temperature dependences of the principal g-factors g_{XY} and g_Z are shown in figures 6(a) and 6(b), respectively, and those of W_{XY} and W_Z are in figure 7(a). g_{XY} and g_Z presented here may be reasonable values for V^{4+}, and they show a slight upturn and downturn at low temperatures, respectively. W_{XY} decreases with decreasing temperature above 70 K, below which it increases. On the other hand, W_Z has a minimum at around 120 K. Below 30 K, both W_{XY} and W_Z increase very rapidly.
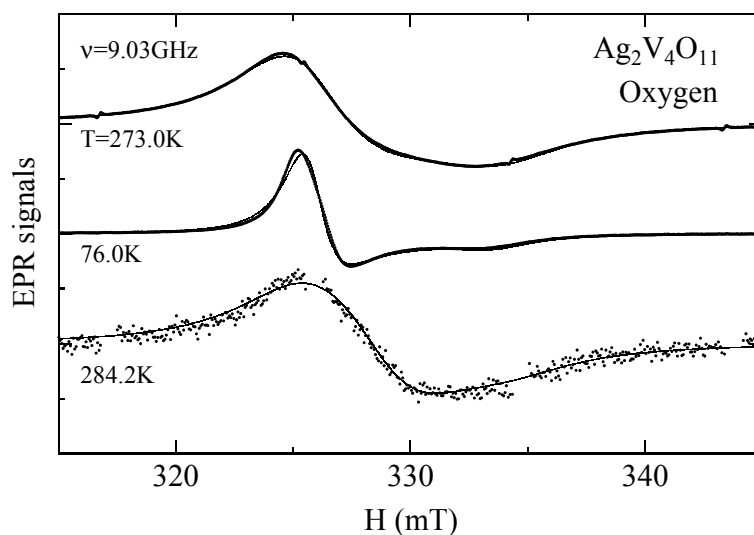

Figure 5. EPR signals of $Ag_2V_4O_{11}$ prepared in an oxygen atmosphere, where the dots and curves represent the experimental and calculated results, respectively. The signals at 273.0 and 76.0 K are those for the polycrystalline specimens, and that at 284.2 K is for the specimens consisting partly of polycrystals and partly of crystals aligned with the c^*-axis.
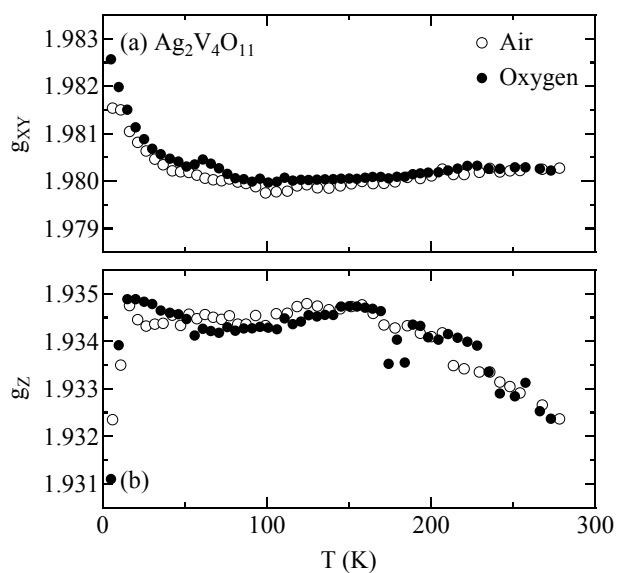
Figure 6. The temperature dependence of the principal *g*-factors ((a) g_{XY} and (b) g_Z) for Ag$_2$V$_4$O$_{11}$ prepared in air and an oxygen atmosphere.
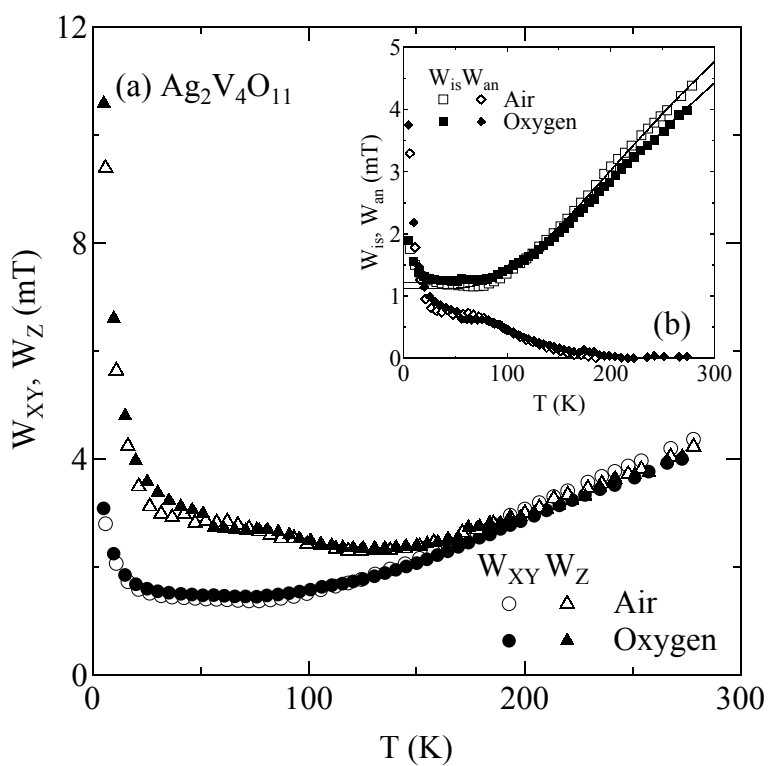

Figure 7. The temperature dependences of (a) the principal EPR linewidths (W_{XY} and W_Z) and (b) the isotropic component (W_{is}) of the linewidth due to just ν_2 and the anisotropic one (W_{an}) directly proportional to ν_1 for Ag$_2$V$_4$O$_{11}$ prepared in air and an oxygen atmosphere. The full curves in (b) show the calculated results for W_{is}.

In order to clarify the direction of the principal axes of the g- and W-tensors, the spectra for specimen (O) which consists partly of polycrystals and partly of crystals aligned with the c^*-axis were measured, since it was impossible to obtain single-domain crystals suitable for measurements. The bottom of figure 5 indicates the result at 284.2 K, which is explained, as shown by the full curve, by an appropriate superposition of the asymmetric spectrum and the symmetric Lorentzian originating from the polycrystals and the aligned ones, respectively. Then, the Z-axis is found to be nearly parallel to the a^*-axis on the assumption that one of the principal axes corresponds to the b-axis on the basis of the crystal symmetry.

The energy-level configuration for V^{4+} may be calculated in terms of a simple perturbation theory of the spin–orbit coupling [21]:

$$\Delta g_i = 2\lambda \sum_n \frac{|\langle n|L_i|0\rangle|^2}{E_n - E_0} \tag{10}$$

where $\Delta g_i = 2.0023 - g_i$; λ is the spin–orbit coupling constant, L_i is the orbital angular momentum operator, and E_n is the energy of the orbital state n. On the basis of the energy levels obtained from the ligand-field analysis, it is found that the g-tensors described above qualitatively correspond to those at the V2 site. Calculating the energy-level configuration with equation (10) for the V2 site with $|0\rangle = d_{yz}$, the energies to the d_{zx}, d_{xy}, and $d_{x^2-y^2}$ states are found to be 100λ, 100λ, and 114λ, respectively.

For the temperature dependence of the linewidth, the random-frequency-modulation model with two characteristic frequencies should be considered. The first frequency ν_1 corresponds to a modulation of the hyperfine interaction A by the electron hopping, which may be reflected in a rapid increase of linewidth at low temperatures. The second frequency ν_2 is responsible for a transition of electrons into a certain excited state, leading to a continuous increase of the isotropic component of the linewidth with increasing temperature. This process becomes predominant at high temperatures. It is noted that ν_1 is larger than A even at the lowest temperature, since hyperfine spectra are not resolved.

The temperature dependence of ν_1 may correspond roughly to that of the anisotropic component of the linewidth defined as $W_{an} = W_Z - W_{XY}$. Moreover, previous EPR work on dilute V^{4+} in V_2O_5 indicates that this ion is at a site with a strong axial anisotropy, and the parameters describing the spectra are $g_{XY} = 1.986$, $g_Z = 1.923$, $A_{XY} = 62 \times 10^{-4}$ cm^{-1}, and $A_Z = 168 \times 10^{-4}$ cm^{-1}, which are reflected in the oxygen coordination [22]. Using these parameters, the isotropic component (W_{is}) of the linewidth originating from just ν_1 is obtained through the relation $W_i = W_{is} + \alpha A_i^2 \nu_1$ with constant α for $i = XY$ and Z. The temperature dependences of W_{is} and W_{an} are shown in figure 7(b). Assuming exponential temperature dependences for ν_1 and ν_2,

$$\nu_1 \propto \exp(-\Delta_1/T) \qquad \nu_2 \propto \exp(-\Delta_2/T) \tag{11}$$

where Δ_1 is the energy for the hopping process and Δ_2 is that for the excited state, they are estimated to be about 10 and 400 K, respectively. The full curves in figure 7(b) show the results calculated for W_{is}. Δ_1 and Δ_2 do not depend on the atmospheric conditions of the sample preparation, and the number of oxygen deficiencies does not have a significant effect on the dynamical properties of the electrons.

The excitation energy Δ_2 revealed from the EPR relaxation is roughly consistent with the energy E_p of the electrical resistivity. The relaxation at microwave frequencies is expected to provide more reliable results for electron transport, and the deviation of E_p for the specimens (A) and (O) in the resistivity measurements matters little. The extremely small value of Δ_1 corresponds to the local electron hopping between localized states under the electrostatic field of the oxygen deficiencies, which is not responsible for the temperature dependence of the resistivity at high temperatures.

4. Conclusions

The crystal structure and the electronic properties of $Ag_2V_4O_{11}$ insertion electrodes have been investigated.

Although the structure determined here is roughly consistent with the previous model, there is a significant difference as regards the oxygen coordinations and the Ag ion, for the present compound is not deficient. $Ag_2V_4O_{11}$ is basically an n-type semiconductor; this may arise from small contents of V^{4+} ions that compensate the oxygen deficiencies. Thus, the V ions are in a V^{5+}–V^{4+} mixed-valence state. The energy-level configuration for the $V2O_6$ octahedra according to the ligand-field calculation qualitatively explains the observed g-tensor. The transport properties are successfully characterized by the small-polaron motion in the localized states of the band tail: at high temperatures, the negative carriers move through thermally excited hopping with a phonon-exchange energy, and at low temperatures, the electron hops between localized states under the electrostatic field of the oxygen deficiencies.

References

[1] For example, Takeuchi E S 1995 *J. Power Sources* **54** 115
[2] Garcia-Alvarado F and Tarascon J M 1994 *Solid State Ion.* **73** 247
[3] West K and Crespi A M 1995 *J. Power Sources* **54** 334
[4] Crespi A M, Skarstad P M, Zandbergen H W and Schoonman 1993 *Proc. Symp. on Lithium Batteries* vols 93–94 (New York: The Electrochemical Society) p 98
[5] Zandbergen H W, Crespi A M, Skarstad P M and Vente J F 1994 *J. Solid State Chem.* **110** 167
[6] Galy J and Lavaud D 1971 *Acta Crystallogr.* B **27** 1005 and references therein
[7] Onoda M and Nagasawa H 1993 *48th Annu. Mtg of the Physical Society of Japan* part 3 (Tokyo: The Physical Society of Japan) abstracts, p 171 (in Japanese)
[8] Kato K, Kosuda K, Saito Y and Nagasawa H 1996 *Z. Kristallogr.* **211** 522
[9] For example, Sanchez C, Henry M, Grenet J C and Livage J 1982 *J. Phys. C: Solid State Phys.* **15** 7133 and references therein
[10] Leising R A and Takeuchi E S 1993 *Chem. Mater.* **5** 738
[11] Sheldrick G M 1985 *Crystallographic Computing* vol 3, ed G M Sheldrick, C Kruger and R Goddard (Oxford: Oxford University Press) p 175
[12] Cromer D T and Waber J T 1974 *International Tables for X-Ray Crystallography* vol 4, ed J A Ibers and W C Hamilton (Birmingham: Kynoch) section 2
[13] Creagh D C and McAuley W J 1992 *International Tables for Crystallography* vol C, ed A J C Wilson (Boston, MA: Kluwer Academic)
[14] teXsan 1992 *Crystal Structure Analysis Package* (The Woodlands, TX: Molecular Structure Corporation)
[15] Zachariasen W H 1978 *J. Less-Common Met.* **62** 1
[16] Freeman A J and Watson R E 1965 *Magnetism* part A, vol 2, ed G T Rado and H Suhl (New York: Academic)
[17] Shannon R D 1976 *Acta Crystallogr.* A **32** 751
[18] Nagels P 1979 *Amorphous Semiconductors* ed M H Brodsky (Springer: New York) p 113
[19] Mott N F 1990 *Metal–Insulator Transitions* 2nd edn (London: Taylor and Francis)
[20] Heikes R R 1961 *Thermoelectricity* ed R R Heikes and R W Ure (New York: Interscience)
[21] Abragam A and Bleaney B 1970 *Electron Paramagnetic Resonance of Transition Ions* (Oxford: Clarendon)
[22] Kahn A, Livage J and Collongues R 1974 *Phys. Status Solidi* a **26** 175